



Electrospinning-based nanofiber architectures for outstanding CO₂ capture

Sangmo Kang^a, Jungho Hwang^{a,*}, Jeong Hoon Byeon^{b,*}

^a School of Mechanical Engineering, Yonsei University, Seoul 03722, Republic of Korea

^b School of Mechanical Engineering, Yeungnam University, Gyeongsan 38541, Republic of Korea

ARTICLE INFO

Keywords:

PEI/CeO₂/ACNFs
CO₂ adsorbent
Electrospinning-based architecting
Simple process manipulation
Electrical polarity

ABSTRACT

The worsening climate change has made the development of alternative and sustainable technologies to achieve carbon neutrality a pressing issue. Numerous strategies for carbon dioxide (CO₂) capture/conversion and relevant material preparation have been dealt with on a case-by-case basis. Therefore, a reconfigurable process to secure optimal procedures and materials is urgently required to reduce CO₂ emissions in a convenient, rapidly implementable manner. On this account, this study attempted to construct polyethylenimine (PEI)/cerium oxide (CeO₂)/activated carbon nanofibers (ACNFs) as a reliable CO₂ adsorbent from an electrospinning (ES)-based architecting as a modular process to accelerate their field applications because adsorption has outstanding advantages for CO₂ capture, such as process simplicity, wide operational range, low cost, and stable performance. By selecting ES with commercially available materials (PEI (providing CO₂ chemisorption), cerium nitrate hexahydrate (CO₂ selectivity), and polyacrylonitrile (base of porous nanofibers)), a composite nanofibrous architecture (PEI/CeO₂/ACNFs) with outstanding CO₂ capture can be achieved by simple process manipulation (manipulating the electrical polarity applied to the nozzle and concentration of the cerium nitrate for the ES). This study may provide a reconfigurable manufacture to ensure a reliable adsorbent for CO₂ capture and base materials for CO₂ conversion from electro- and photocatalysis.

1. Introduction

Climate change is recognized as a critical global issue by most people around the world [1]. Recently, it has been suggested that the carbon dioxide (CO₂) concentration is related directly to the ecosystem and biodiversity of the air and the ocean as an air filter of the world [2]. Advanced adsorption materials are essentially required as an active alternative to reducing CO₂ [3]. On the other hand, only limited data or complex approaches for highly capacitive and selective adsorption have been provided a case-by-case basis, and there is a lack of sufficient information, even for workable architectures of adsorbents. In that sense, a high-throughput screening platform is required as a priority to accelerate the utilization of reliable CO₂ adsorbents for practical applications.

As a primary viable option to capture CO₂, adsorption using porous materials, such as metal–organic frameworks (MOFs) [4], zeolites [5], porous polymer networks [6], and porous carbon [7], has been considered because of convenience, material abundance, simple facility, and low cost and energy consumption. On the other hand, surface modifications based on hydrothermal or vacuum (sputtering for nanoroughness or vapor deposition for functional overlayers) reactions are

required to ensure enhanced adsorption capacity considering adsorbate species, operating temperature and pressure, and space velocity [8,9]. A trade-off problem between the higher performance and process complexity may impede the practical applications of developed materials for CO₂ reduction. A convenient, modular, high-yield platform is required to screen architectures systematically for reliable CO₂ adsorption.

Because of the “mix and go” convenient configuration, electrospinning (ES) has been used extensively to produce a diverse spectrum of nanofibrous nonwovens for separation and purification purposes in the past three decades [10]. Nanofibrous structures can be installed in most environmental pollutant treatment plants because of their proper architecture, flexibility, and textural property with tolerable pressure drop. These can be extendable for energy production and storage applications [11,12]. An electric potential with polarity modulation on the spinning nozzle can control the arrangement of ionic compounds (directly added to the polymeric precursor for functionalizing/modifying purposes) in the discharging of a mixture precursor [13,14] that conveniently generates various composite nanofibers with no post-treatments under harsh hydrothermal or vacuum conditions [15].

* Corresponding authors.

E-mail addresses: hwangjh@yonsei.ac.kr (J. Hwang), postjb@yu.ac.kr (J.H. Byeon).

<https://doi.org/10.1016/j.seppur.2023.124202>

Received 12 March 2023; Received in revised form 14 May 2023; Accepted 24 May 2023

Available online 27 May 2023

1383-5866/© 2023 Elsevier B.V. All rights reserved.

Subsequent thermal carbonization and activation formed textures in the resulting nanofibers to secure micro- and mesoporosity, whereas utilizing this technique is still immature for CO₂ adsorption.

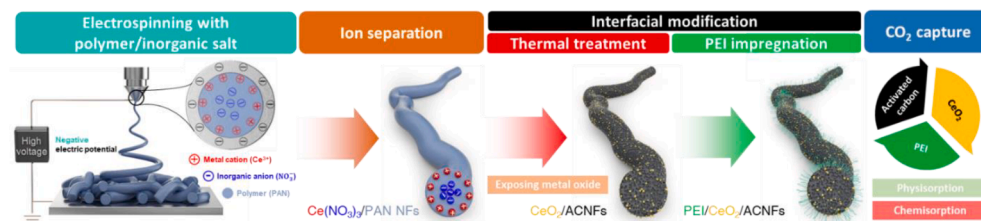
This paper proposes an ES-based platform to build an overlayer/interlayer/base fiber (securing compositional hierarchy) architecture for highly capacitive, reliable CO₂ adsorption, where polyethylenimine (PEI; providing CO₂ chemisorption), cerium dioxide (CeO₂; CO₂ selectivity), and activated carbon nanofibers (ACNFs; base for adsorption capacity) were selected as the individual layer materials by successive ES, thermal treatment, and bath immersion (Fig. 1). The polarity of the electric potential and concentration of CeO₂ precursor (cerium nitrate hexahydrate (Ce(NO₃)₃), a Ce³⁺ source) were selected as vital parameters to ensure modular property and control the arrangement and density of Ce³⁺ for screening optimal interlayer/base fiber (CeO₂/ACNFs) architecture upon a thermal treatment for CO₂ adsorption. Subsequent immersion of the CeO₂/ACNFs in the PEI bath for impregnating amine groups (constructing a PEI/CeO₂/ACNFs hierarchy) was conducted to reinforce the chemisorption of the adjacent CO₂.

2. Experimental

2.1. ES-based construction

Cerium nitrate hexahydrate (CAS#10294-41-4; Ce(NO₃)₃ • 6H₂O) with different doses (0.05, 0.10, 0.15, and 0.20 g) was dissolved in 10 mL of N,N-dimethylformamide (CAS#68-12-2; DMF) and stirred for 1 h at 60 °C. The solution was then incorporated with 1 g of polyacrylonitrile (PAN; CAS#25014-41-9; *M_w* = 150,000 g/mol) for one day with magnetic stirring at room temperature to form Ce(NO₃)₃/PAN composite precursors. The resulting precursor solutions were fed into a plastic syringe for ES at a flow rate of 5 μL min⁻¹, which was regulated using a syringe pump (Fig. S1). The metal nozzle (inner diameter = 0.67 mm) was connected to an electric potential of -12 kV, where the distance between the tip of the nozzle and the revolving drum collector (200 rpm) was 15 cm. The diameter and length of the drum collector were 10 and 20 cm, respectively. As shown in Fig. S2, the as-spun NFs were put in an alumina tube and treated thermally through the following steps: (1) stabilization (250 °C), (2) carbonization (250–900 °C), (3) activation (900 °C), and (4) oxidation (250 °C). The thermally treated NFs were denoted as CeO₂/ACNFs-1–4. For comparison, analogous NFs were synthesized without cerium nitrate (ACNFs) or under the opposite electric polarity (+12 kV; +CeO₂/ACNFs).

To prepare PEI-impregnated samples, 2 g of vacuum-dried (at 150 °C for 12 h) ACNFs was immersed in a PEI (*M_w* = 800 Da) solution (10 g PEI dissolved in 200 mL of ethanol for 1 h under magnetic stirring) and stirred magnetically at room temperature for 3 h to ensure the PEI impregnation on the sample surfaces (approximately 0.85 g of PEI/1.00 g of ACNFs). The treated sample was placed in a vacuum oven at 100 °C for 5 h to secure dried PEI/ACNFs. An analogous procedure was carried out for CeO₂/ACNFs and +CeO₂/ACNFs to provide PEI/CeO₂/ACNFs and PEI/+CeO₂/ACNFs.



discharging precursor solution (Ce(NO₃)₃/PAN in DMF). The dose of was Ce(NO₃)₃ regulated in the four stages to ensure optimal distribution of CeO₂ particles and pore size of ACNFs. The as-spun nanofibers (Ce(NO₃)₃/PAN NFs) were thermally treated to produce CeO₂ particles on porous nanofibers (CeO₂/ACNFs), and subsequently immersed in PEI solution to form PEI-impregnated CeO₂/ACNFs (PEI/CeO₂/ACNFs) for their use in CO₂ adsorption tests.

2.2. CO₂ adsorption

A static volumetric analyzer (TriStar II 3020, Micromeritics, USA) was used to obtain the capacities of CO₂ adsorption for the resulting samples. Before the test, the samples were degassed for 12 h at 150 °C to remove moistures (ensuring the residual pressure of <1 × 10⁻³ mbar). A steady flow of CO₂ (0.015 L/min) was used to test each sample (0.1 g), while different temperatures (0, 25, 50, and 75 °C) were conducted to examine the adsorption capacity. The nitrogen (N₂) adsorption capacity was also examined under identical conditions to identify the selectivity of CO₂ adsorption. The CO₂ desorption was conducted at 100 °C for 2 h under pure nitrogen (as desorption gas) atmosphere.

2.3. Characterization

The samples were examined by field-emission scanning electron microscopy (SEM; 7800F, JEOL, Japan) and transmission electron microscopy (TEM; JEM-F200, JEOL, Japan). Elemental maps were obtained using an energy-dispersive X-ray spectroscopy (EDS) included in the TEM. To prepare the specimens, ethanol was used to disperse each sample before placing it on a carbon-coated copper grid. The crystallinity of the samples was analyzed by X-ray diffraction (XRD; SmartLab, Rigaku, Japan) with a Cu Kα radiation source. X-ray photoelectron spectroscopy (XPS; K-Alpha, Thermo Scientific, USA) was used to obtain the Ar⁺ depth profiles with an etching rate of 0.1 nm/s for quantifying the surface elements of the samples. The surface chemistry and pyrolysis characteristics were examined using Fourier transform infrared (FTIR) spectroscopy (VERTEX 70, Bruker, USA) and thermogravimetric analysis (TGA; LABSYS evo, Setaram Instrumentation, France), respectively. The textural properties of the samples were analyzed using a porosimeter (Autosorb-iQ 2ST/MP, Quantachrome, Austria).

3. Results and discussion

Different doses of the inorganic salt (Ce(NO₃)₃ • 6H₂O) were mixed individually with PAN in DMF to produce precursor solutions for constructing CeO₂/ACNFs-1, CeO₂/ACNFs-2, CeO₂/ACNFs-3, and CeO₂/ACNFs-4. An external electric potential with different polarities (+, -) was applied to derive the electrohydrodynamic movement of the ionic compounds in the precursor solution during its discharging through the ES nozzle. For the negative potential, Ce³⁺ and NO₃⁻ ions migrated toward the outer and inner regions of the nozzle, respectively, while the ions moved in opposite directions with the positive potential (Fig. 2A and 2B). The figures also present representative SEM images of the electrospun Ce(NO₃)₃/PAN fibers under negative and positive electric potentials. Both fibers showed smooth surfaces with a diameter range from 250 to 300 nm.

The concentrations of Ce³⁺ (C_i) as a function of the distance from the center of the nozzle (x) were determined analytically using the Boltzmann distribution and zeta potential profile equations (Eqs. S1 and S2) [16]. Ce³⁺ was distributed narrowly with distance from the center of the nozzle, where the concentrations were dependent on the electrical

Fig. 1. Schematic of the ES-based process to construct hierarchical composite nanofibers for reliable CO₂ adsorption from a combined physi- and chemisorption. To ensure a proper distribution of Ce³⁺ ions within PAN, different polarities (+ and -) of electric potential were applied to the ES nozzle, where the ion pairs (Ce³⁺ and NO₃⁻) from the dissolution of Ce(NO₃)₃ were oppositely moved by switching the polarity that generates different distributions of the ion pairs within

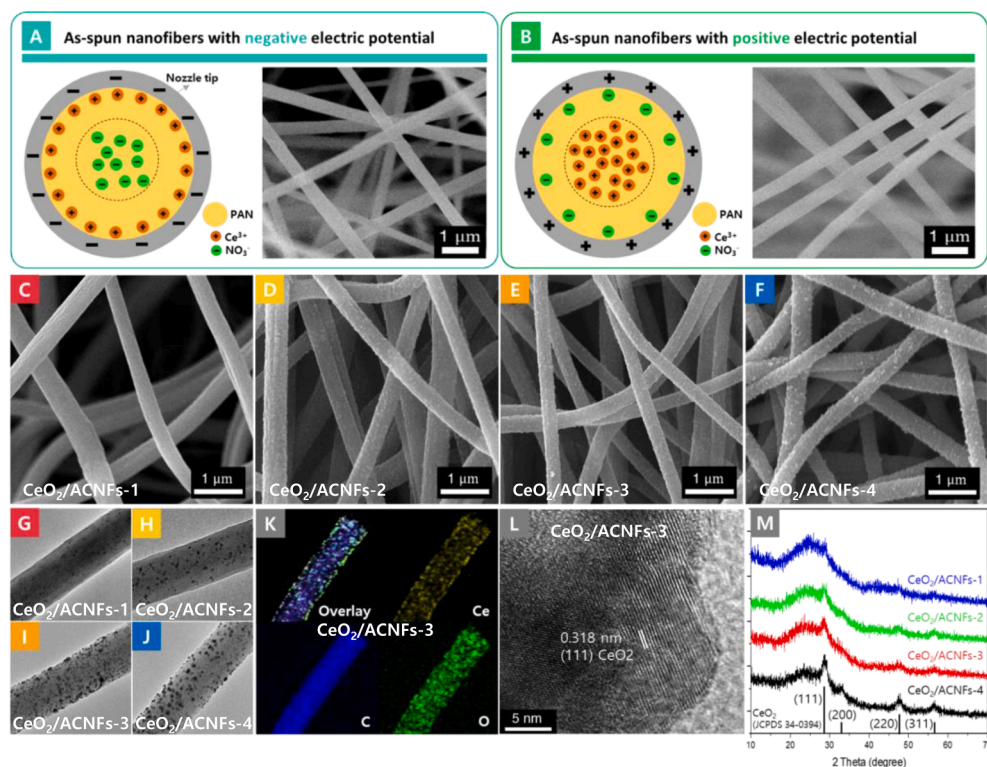


Fig. 2. Schematics of the ion pair distribution for different electrical polarities and the resulting morphology, microstructure, and composition of $\text{CeO}_2/\text{ACNFs}$. (A, B) SEM images of as-spun fibers from the positive and negative electric potentials for ES of $\text{Ce}(\text{NO}_3)_3/\text{PAN}$ solution. (C–F) SEM images of $\text{CeO}_2/\text{ACNFs}$ from the four doses of $\text{Ce}(\text{NO}_3)_3$ to examine the formation of particles on the fiber surfaces. (G–J) The corresponding TEM images. (K) Representative EDS maps of $\text{CeO}_2/\text{ACNFs}$ -3. (L) High-magnification TEM image of the outermost region of $\text{CeO}_2/\text{ACNFs}$ -3 to identify the microstructures of the fiber and particle simultaneously. (M) XRD profiles $\text{CeO}_2/\text{ACNFs}$ from the four doses of $\text{Ce}(\text{NO}_3)_3$ to confirm the crystallinities of the fiber and particle with those in the TEM image.

polarity and strength, as shown in Fig. S3A and S3B. In particular, the ions were densely distributed ($>450 \text{ M}$) at a distance of 160 to 180 nm for the negative potential. Longer distances (i.e., closer to the fiber surface) were obtained at higher electric strengths because of the stronger electrostatic attractions between the Ce^{3+} and the negatively charged nozzle surface. By contrast, relatively negligible amounts of ions were distributed at these distances because of electrostatic repulsion, showing that modulating the electric polarity was the driver for the concentrated distribution of Ce^{3+} in the outer or inner region of the fibers. The atomic depth profiles Fig. S3C from argon ion (Ar^+) etching matched the surface concentrated distribution of Ce^{3+} (6.6%) for the negative potential (cf., nearly zero % for the positive potential), supporting the adjustability of the ES for the site-selective distribution of Ce^{3+} . FTIR spectroscopy showed a significantly greater surface distribution of NO_3^- (absorption band at $1380\text{--}1350 \text{ cm}^{-1}$) for the positive potential [17], as shown in Fig. S4.

With regard to morphology, the thermally treated samples ($\text{CeO}_2/\text{ACNFs}$ -1 to $\text{CeO}_2/\text{ACNFs}$ -4) exhibited a fine roughness from small particles (brighter dots) on the fiber surfaces (Fig. 2C–2F) unlike the as-spun fibers. The roughness was caused by oxidation of the outermost Ce^{3+} ions (forming CeO_2 particles) with shrinkage of the PAN fibers during thermal treatment. Different doses of the cerium nitrate induced different distributions of CeO_2 particles on the fiber surfaces, where the density and size of the particles were proportional to the dose of $\text{Ce}(\text{NO}_3)_3$, as observed by TEM (Fig. 2G–2J). EDS maps of the $\text{CeO}_2/\text{ACNFs}$ -3 revealed the co-existence of Ce and O on a single carbon fiber (Fig. 2K), while the characteristic lattice spacing (0.318 nm) for CeO_2 , (111) was identified by high-magnification TEM (Fig. 2L). XRD (Fig. 2M) revealed the characteristic 2θ bands at 28.6° , 33.1° , 47.6° , and 56.3° , which were indexed to the (111), (200), (220), and (311) lattice planes of CeO_2 , respectively [18]. A broad diffraction band at approximately 25° was assigned to amorphous carbon formed from the thermal treatment of PAN [19]. The intensity of the characteristic CeO_2 bands was also proportional to the $\text{Ce}(\text{NO}_3)_3$ dose, which is consistent with the size increases in TEM images (Fig. 2G–2J) by estimating the average crystal sizes using the Scherrer equation (Table S1). For comparison, the

morphologies of ACNFs and $+\text{CeO}_2/\text{ACNFs}$ -3 were observed by SEM and TEM, where no dark dots on the fiber surfaces were identified (Fig. S5). There were no significant differences in appearance between ACNFs (Fig. S5A) and $+\text{CeO}_2/\text{ACNFs}$ -3 (Fig. S5C). On the other hand, the TEM image of $+\text{CeO}_2/\text{ACNFs}$ -3 exhibited fine dark dots in the core region, which may be caused by the inside-concentrated distribution of Ce^{3+} ions for the positive potential. The dots were smaller than those of $\text{CeO}_2/\text{ACNFs}$ -3 probably due to limited oxygen exposure to the inner region located Ce^{3+} ions to form CeO_2 particles that generate weak intensities of the characteristic CeO_2 bands compared to those of $\text{CeO}_2/\text{ACNFs}$ -3 despite the differences between the ACNFs and $+\text{CeO}_2/\text{ACNFs}$ -3 (Fig. S6). This represented that the inside-dominant distribution of Ce^{3+} could retain surface texture of ACNFs likely due to the confined oxidation of Ce^{3+} ions to form CeO_2 particles.

The thermal decomposition behavior of $\text{Ce}(\text{NO}_3)_3/\text{PAN}$ NFs (as-spun prior to ACNFs, $+\text{CeO}_2/\text{ACNF}$ -3, and $\text{CeO}_2/\text{ACNFs}$ -3) was investigated by TGA in steps 1 and 2 of the thermal treatment (Fig. S2). As shown in Fig. S7, the weight losses in the temperature range ($25\text{--}250^\circ\text{C}$) in the air atmosphere resulted from the cyclization of nitrile groups and dehydrogenation of PAN (i.e., the stabilization of PAN) [20]. Until the temperature reached 250°C , the as-spun fiber samples exhibited weight losses of 1.17%, 2.52%, and 3.95%, respectively. Additional weight losses (2.42%, 2.96%, and 4.29%) were observed when the temperature was maintained at 250°C for 30 min. The highest weight loss of $\text{Ce}(\text{NO}_3)_3/\text{PAN}$ may be caused by the catalytic oxidation of adjacent PAN molecules, which was induced by oxidation of the outermost Ce^{3+} to CeO_2 . The higher loss of $+\text{Ce}(\text{NO}_3)_3/\text{PAN}$ than PAN reflected this hypothesis. This is consistent with a previous report where a significant shrinkage of PAN was observed upon oxidation of transition metal to metal oxide in PAN during thermal treatment [21]. Over 250°C with a nitrogen atmosphere, the samples exhibited nearly identical weight loss profiles, where the losses were mostly driven by pyrolytic carbonization of PAN. The weight differences between the samples were similar during the temperature increase, suggesting that no more catalytic oxidation of the PAN occurred because of a lack of oxygen molecules. After the temperature reached 900°C , the residues of the PAN, $+\text{Ce}(\text{NO}_3)_3/\text{PAN}$,

and $\text{Ce}(\text{NO}_3)_3/\text{PAN}$ were 32.65%, 31.19%, and 29.53%, respectively, which were probably due to pyrolysis-induced shrinkage in the absence of oxygen.

Textural properties of the thermally treated CeO_2/ACNF samples (1–4), including ACNFs and $+\text{CeO}_2/\text{ACNF}$ -3, were obtained from N_2 adsorption–desorption isotherms using the Brunauer–Emmett–Teller (BET) method. As shown in Fig. 3A, all samples exhibited a substantial increase in N_2 adsorption at a low relative pressure (<0.05), representing a significant portion of micropores. In particular, ACNFs demonstrated type-I isotherms, whereas the others (CeO_2 -containing configurations) exhibited type-IV isotherms with H_4 hysteresis loops in the range of 0.5–1.0 (P/P_0) due to the mesoporosity of slit-shaped pore channels owing to CeO_2 formation [22]. The N_2 adsorption capacity of the samples was observed in the following order: $\text{CeO}_2/\text{ACNFs}$ -4 $<$ ACNFs $<$ $\text{CeO}_2/\text{ACNFs}$ -1 $<$ $\text{CeO}_2/\text{ACNFs}$ -2 $<$ $\text{CeO}_2/\text{ACNFs}$ -3. Even though increasing $\text{Ce}(\text{NO}_3)_3$ content in PAN led to improvement of the adsorption performance, an excessive dose of $\text{Ce}(\text{NO}_3)_3$ caused the formation of unfavorable architecture (forming larger CeO_2 particles and their blocking the pore channels) for transport within the microstructure and interaction with CeO_2 and ACNF surface of CO_2 molecules. The lowest capacity of $\text{CeO}_2/\text{ACNFs}$ -4 may be due to the blockage of slit-shaped pores by the densest distribution of CeO_2 particles on the fibers, which could be confirmed by the modulation of $\text{Ce}(\text{NO}_3)_3$ doses.

The pore size distributions of the samples were determined using the Barrett–Joyner–Halenda (BJH) and Horvath–Kawazoe (HK) models. As shown in Fig. S8, drastic increases in pore volume were observed for the diameters smaller than 3 nm in all samples, showing that the thermal treatment induced a significant portion of micropores. On the other hand, $\text{CeO}_2/\text{ACNFs}$ -2, 3, and 4 included relatively larger portions of the pores with diameters >3 nm because of the coexistence of the mesoporous CeO_2 particles (Table S1). The highest volume of $\text{CeO}_2/\text{ACNFs}$ -3 matched the N_2 adsorption capacity, suggesting that modular coordination of Ce^{3+} is required to ensure optimal textural properties. The pore size distributions for diameters <1 nm were also analyzed to identify the portion of pores with diameters of 0.5 to 0.6 nm (Fig. 3B) because these diameters (close to the kinetic diameters (<1 nm) of CO_2) are favorable for physical adsorption of CO_2 (increasing adsorption energy of CO_2 due to van der Waals potential field formed by the pore walls) [23,24]. Compared to the others, $\text{CeO}_2/\text{ACNFs}$ -3 exhibited a prominent portion of the pores for CO_2 selectivity, showing the requirement of the modular approach to derive a favorable effect of the simultaneous oxidation of Ce^{3+} ions and PAN molecules for constructing optimal textural properties.

The textural properties of PEI-impregnated (for reinforcing CO_2 chemisorption) $\text{CeO}_2/\text{ACNFs}$ -3 (PEI/ $\text{CeO}_2/\text{ACNFs}$ -3), including PEI/ACNFs and PEI/ $+\text{CeO}_2/\text{ACNFs}$ -3 were also investigated. All samples exhibited significantly reduced N_2 adsorption after impregnation,

reflecting that the PEI was loaded on the nearly entire the pore walls through the simple immersion (Fig. S9A). The lower N_2 adsorption levels at low relative pressures represented the PEI loading on most of the micropore region upon impregnation. The CeO_2 -included samples still exhibited type-IV isotherms even after PEI incorporation, suggesting that the loading was performed uniformly along the pore walls. The stronger hysteresis intensity at $>0.5 P/P_0$ for PEI/ $\text{CeO}_2/\text{ACNFs}$ -3 than PEI/ $+\text{CeO}_2/\text{ACNFs}$ -3 was related to the higher amount of CeO_2 particles on the fiber surfaces. On the other hand, the loading changed the type of the hysteresis loop from H_4 to H_3 , which followed the existence of non-rigid aggregates of CeO_2 particles, according to a previous report [25]. Although $\text{CeO}_2/\text{ACNFs}$ retained the CO_2 selective microporosity after the loading, the micropore volumes in both BJH (Fig. S9B) and HK (Fig. S9C) models were reduced significantly. PEI/ $+\text{CeO}_2/\text{ACNFs}$ showed a similar pore size distribution to PEI/ACNFs than PEI/ $\text{CeO}_2/\text{ACNFs}$, suggesting that the insufficiently developed CeO_2 on the fiber surface cannot generate favorable textures for CO_2 adsorption. The PEI loading was analyzed further by FTIR (Fig. S10), where the C=O and C–N stretching vibrations of the amide were observed at 1620 and 1575 cm^{-1} , respectively, as an amine-grafted architecture [26]. Unlike the $\text{Ce}(\text{NO}_3)_3/\text{PAN}$ NFs, the strong absorption bands at 1581 cm^{-1} and 1251 cm^{-1} were assigned to C=C and C–C bonds instead alkyl, nitrile, carbonyl, and ether groups, also proving successful carbonization of PAN NFs through the thermal treatment [27].

Fig. 4A and S11 show the CO_2 and N_2 adsorption capacities and the equilibrium isotherms of ACNFs, $\text{CeO}_2/\text{ACNFs}$ -3, PEI/ACNFs, PEI/ $+\text{CeO}_2/\text{ACNFs}$ -3, and PEI/ $\text{CeO}_2/\text{ACNFs}$ -3 at different temperatures for pressure up to 850 mmHg (1.13 bar), respectively. The adsorption capacities of all samples were proportional to pressure, which were due to the forced deep diffusion of CO_2 into the pores regardless of PEI incorporation. In the absence of PEI (ACNFs and $\text{CeO}_2/\text{ACNFs}$ -3), CO_2 adsorption was inversely proportional to the operating temperature, showing exothermic physisorption to be the main driver of the CO_2 uptake (Fig. S11A and S11B). The higher uptake for $\text{CeO}_2/\text{ACNFs}$ -3 than ACNFs proved that the formation of CeO_2 particles on the surface of activating NFs could provide a favorable pore structure and selectivity for enhanced CO_2 adsorption. The microstructure of the resulting CeO_2 particles may also have oxygen basic and vacant sites as active surfaces that enable the storage of extra oxygen. These oxygen vacancies may act as active sites for the chemisorption and activation of CO_2 , leading to the reduction to CO or other products from intermediate carbonates [28]. Owing to the presence of the active sites with adjacent hydroxyl groups, adsorbed CO_2 onto the active sites was reacted with surface oxygen ions or hydroxide species to be formed as carbonates [29,30]. This suggests that $\text{CeO}_2/\text{ACNFs}$ -3 may provide greater selectivity to CO_2 than N_2 ($<5 \text{ cm}^3/\text{g}$ at 0°C , 850 mmHg) owing to its large quadrupole moments and polarizability to CO_2 molecules [31]. In the presence of PEI

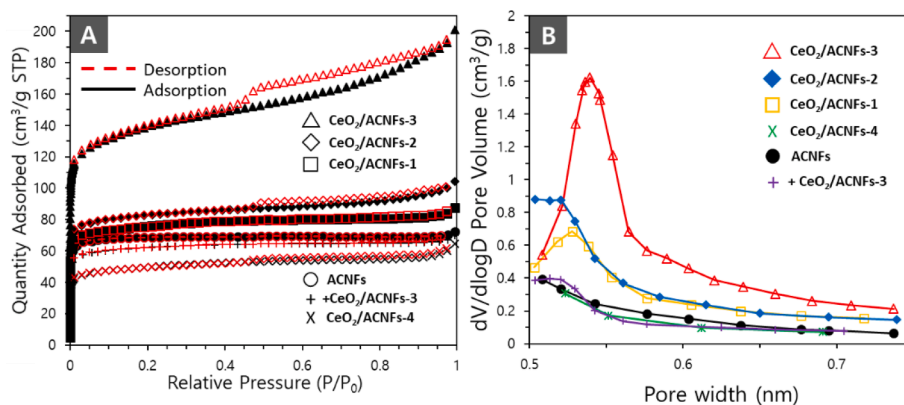


Fig. 3. Textural properties of the resulting $\text{CeO}_2/\text{ACNFs}$ from the four doses of $\text{Ce}(\text{NO}_3)_3$, including ACNFs and $+\text{CeO}_2/\text{ACNFs}$ -3 for comparison. (A, B) N_2 adsorption–desorption isotherms and pore size distributions (from the HK model) of the samples.

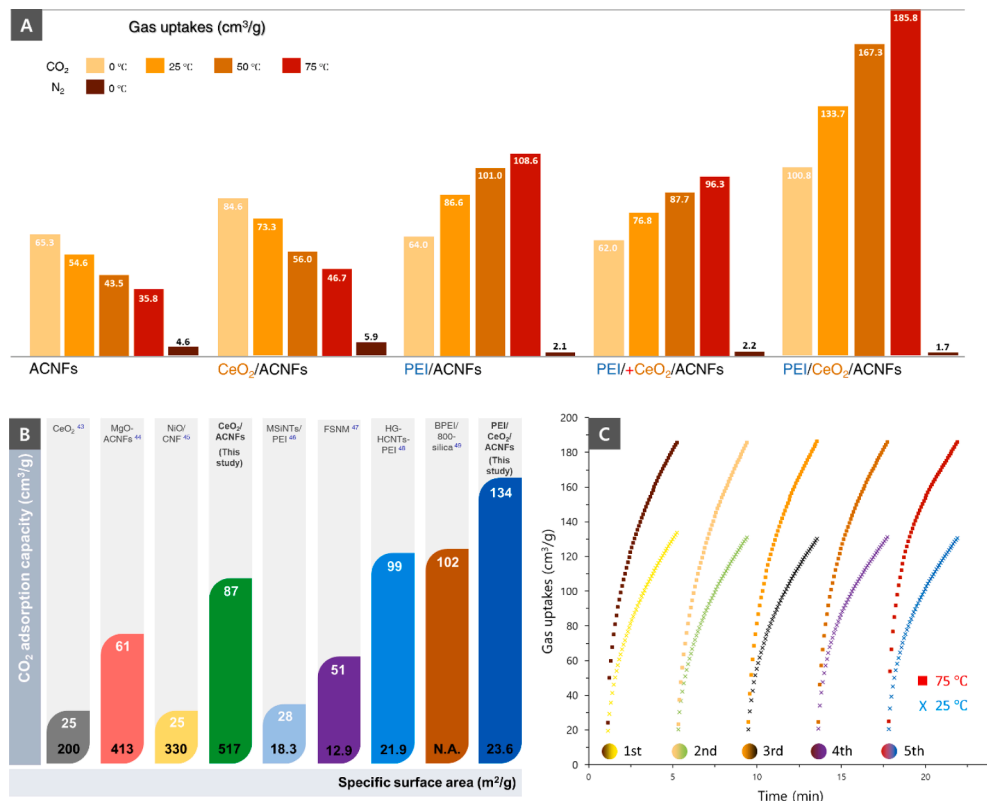


Fig. 4. CO₂ adsorption performance and stability at different operating temperatures. (A) CO₂ adsorption capacities of the samples in the absence (ACNFs, CeO₂/ACNFs-3) and presence (PEI/ACNFs, PEI/CeO₂/ACNFs-3, and PEI/CeO₂/ACNFs-3) of PEI at 850 mmHg. The figure includes N₂ adsorption results for comparison. (B) Comparison in the adsorption capacity between the present and previous studies with and without PEI. (C) Cyclability of PEI/CeO₂/ACNFs-3 for five consecutive CO₂ adsorption tests at 25 °C and 75 °C. After each cycle, the sample was degassed at 100 °C for 1 h in dry air.

(Fig. S11C–S11E), PEI/CeO₂/ACNFs-3 exhibited the highest CO₂ adsorption capacity (reached 185.79 cm³/g at 75 °C, 850 mmHg; derived the highest Q_{\max} in the Langmuir–Freundlich model (Table S2 and Eqs. S3 and S4)), even better than those in most recent relevant studies [32]. This highest performance was probably due to a combinatorial effect of chemical and physical CO₂ affinities of PEI and CeO₂ from the optimal CeO₂ particle and pore size distributions that confers enhanced bindings to adjacent CO₂ molecules, even under lower operating pressures (<100 mmHg) [33]. Other bindings from electrostatic (between the positively charged groups in PEI and negatively charged CeO₂), Lewis acid (CeO₂)–base (PEI), and π – π stacking (between the aromatic groups on PEI and ACNF) interactions might also derive the enhancement in CO₂ adsorption [34–36]. In the case of PEI/ACNFs, the higher capacities than those of ACNFs alone at higher temperatures were related to the strong interactions between the CO₂ and amine groups of PEI on the microporous channels of ACNFs. The temperature-dependent uptake manner was attributed to the increased molecular flexibility and intermolecular distance of the branched chain of PEI molecules, promoting the reactivity with CO₂ [37–39]. The PEI-impregnated CeO₂/ACNFs-3 also exhibited the temperature-dependent manner, suggesting that the PEI/CeO₂/ACNFs hierarchical architectures may be a viable option even for post-combustion CO₂ capture [7,32]. As shown in Fig. S11A–S11E, the Freundlich and Langmuir–Freundlich models were well fitted ($R^2 > 0.99$) to the experimental results of CO₂ adsorption for all tested samples (Table S2). In particular, the operating temperatures were relevant (inversely or directly proportional) to the value of n (determined by the slope of the plot in the Freundlich model) [40], while all of the n values in the Freundlich model were >1 , representing the favorable multilayer adsorption of CO₂ [41].

Fig. S11F and Table S3 (with Eqs. S5 and S6) present the van't Hoff plot and thermodynamic parameters of ΔH° , ΔS° , and G° of the samples, respectively. The negative values of ΔH° in the absence of PEI (ACNFs and CeO₂/ACNFs-3) confirmed the exothermic nature of the adsorption process, driven by a net decrease in entropy. The higher ΔH° level of CeO₂/ACNFs-3 than ACNFs indicated that CeO₂/ACNFs-3 has a greater

portion of chemisorption. The inversely proportional adsorption capacity of ACNFs and CeO₂/ACNFs-3 to the operating temperature reflected the increases in ΔG° with increasing temperature, which matched the CO₂ uptake results (Fig. S11A and S11B). In the presence of PEI, the positive ΔH° values of the samples represented an endothermic adsorption process for CO₂, indicating better performance at high temperatures. On the other hand, the momentum to offset the CO₂ adsorption will be strengthened due to the exothermic nature of CO₂ adsorption that accelerates the desorption of CO₂ as the temperature increases. This induced relatively lower R^2 levels (dependence on the van't Hoff equation in the CO₂ adsorption) for PEI/ACNFs ($R^2 = 0.8051$) and PEI/CeO₂/ACNFs-3 ($R^2 = 0.4883$) that that of PEI/CeO₂/ACNF-3 ($R^2 = 0.9432$), proving the robust performance of PEI/CeO₂/ACNF-3 in a temperature-dependent manner.

Fig. 4B shows a comparison in CO₂ adsorption capacity between the present and previous studies in the absence and presence of PEI [42–48]. The developed CeO₂/ACNFs-3 and PEI/CeO₂/ACNFs-3 in this study demonstrated the highest specific surface area and CO₂ adsorption capacity within each category. The consecutive CO₂ adsorption–desorption tests were also carried out at different temperatures (25 °C and 75 °C) to investigate the cycling behavior and stability of PEI/CeO₂/ACNFs-3 (Fig. 4C). The adsorption capacity of PEI/CeO₂/ACNFs-3 exhibited relatively constant capacities at 25 °C (130–134 cm³/g) and 75 °C (185–187 cm³/g) after the five adsorption–desorption cycles. This stability was probably due to PEI overlayers as protective coatings to suppress the deactivation of CeO₂ particles on the fiber surface, further suggesting that the overlayer (PEI)/interlayer (CeO₂)/base fiber (ACNFs) hierarchical architecture warrants further investigation for its practical applications.

In the light of practical implementation, the necessary expense for the proposed method was estimated based on a previous study [49], which was compared to that from chemical surface etching of Ce(NO₃)₃/PAN NFs for surface distribution of Ce components. Even though the cost reduction by adopting the proposed method was marginal for the PEI/CeO₂/ACNFs production, wastewater generation and chemicals to be

consumed for the chemical etching can be reduced by switching the electrical polarity for electrospinning. Nevertheless, the cost issue of Ce (NO₃)₃ needs to be compromised through mass production and improving supply chain stability to secure an actual competitive advantage in practical implementation [50].

4. Conclusion

To ensure an optimal compositional hierarchy of nanofibrous adsorbents for CO₂ emissions, an ES-based assembly with polarity modulation of electric potential was developed and utilized to build composite architectures. In particular, the location of Ce³⁺ in the Ce(NO₃)₃/PAN precursor (inner distribution at positive potential while outer at a negative potential) was conveniently manipulated by switching electrical polarity when the precursor was discharged through the nozzle with electric potential. At a negative potential, in particular, CeO₂ particles were densely distributed on the surface of the nanofibers as CeO₂/ACNFs after the thermal treatment. Their distribution was optimized by regulating the deployed Ce³⁺ concentration to enhance CO₂ adsorption superior to previous studies. Anchoring PEI molecules onto CeO₂/ACNFs further enhanced CO₂ adsorption even at increased temperature probably because of the capacity of CO₂ chemisorption to ACNFs. Switching polarity of the electrical potential for electrospinning was effective to distribute conveniently CeO₂ particles on ACNFs to maximize CO₂ adsorption capacity while only an immersion of CeO₂/ACNFs in PEI dissolved solution was required to anchor PEI molecules for improving chemisorption of CO₂ in spite of the porosity reduction. A repetitive adsorption–desorption of CO₂ proved the stability in high temperature and long-term operation. This work may provide a reliable architecture of highly capacitive composite nanofibers for CO₂ capture and modular preparation platform to screen optimal hierarchies of base adsorbents for various types of CO₂ capture and conversion applications.

CRedit authorship contribution statement

Sangmo Kang: Methodology, Validation, Formal analysis, Investigation, Data curation, Writing – original draft. **Jungho Hwang:** Methodology, Validation, Funding acquisition, Writing – review & editing, Project administration, Supervision. **Jeong Hoon Byeon:** Methodology, Validation, Data curation, Conceptualization, Writing – review & editing, Project administration, Supervision.

Declaration of Competing Interest

The authors declare that they have no known competing financial interests or personal relationships that could have appeared to influence the work reported in this paper.

Data availability

Data will be made available on request.

Acknowledgements

This work was supported by Korea Environment Industry & Technology Institute (KEITI) through Technology Development Project for Biological Hazards Management in Indoor Air Program, funded by Korea Ministry of Environment (MOE) (2021003370005). This work was also supported by Korea Environment Industry & Technology Institute (KEITI) through Core Technology Development Project for Environmental Diseases Prevention and Management, funded by Korea Ministry of Environment (MOE) (ARQ202201527001).

Appendix A. Supplementary data

Supplementary data to this article can be found online at <https://doi.org/10.1016/j.seppur.2023.124202>.

References

- [1] K. Rennert, F. Erickson, B.C. Prest, L. Rennels, R.G. Newell, W. Pizer, C. Kingdon, J. Wingenroth, R. Cooke, B. Parthum, D. Smith, K. Cromar, D. Diaz, F.C. Moore, U. K. Müller, R.J. Plevin, A.E. Raftery, H. Ševčíková, H. Sheets, J.H. Stock, T. Tan, M. Watson, T.E. Wong, D. Anthoff, Comprehensive evidence implies a higher social cost of CO₂, *Nature* 610 (2022) 687–692, <https://doi.org/10.1038/s41586-022-05224-9>.
- [2] J. Uetake, T.C.J. Hill, K.A. Moore, P.J. DeMott, A. Protat, S.M. Kreidenweis, Airborne bacteria confirm the pristine nature of the Southern Ocean boundary layer, *Proc. Natl. Acad. Sci. U.S.A.* 117 (2020) 13274–13282, <https://doi.org/10.1073/pnas.2000134117>.
- [3] J.Y. Lai, L.H. Ngu, S.S. Hashim, A review of CO₂ adsorbents performance for different carbon capture technology processes conditions, *Greenh. Gases Sci. Technol.* 11 (2021) 1076–1117, <https://doi.org/10.1002/ghg.2112>.
- [4] M.-H. Yu, P. Zhang, R. Feng, Z.-Q. Yao, Y.-C. Yu, T.-L. Hu, X.-H. Bu, Construction of a multi-cage-based MOF with a unique network for efficient CO₂ capture, *ACS Appl. Mater. Interfaces* 9 (2017) 26177–26183, <https://doi.org/10.1021/acsami.7b06491>.
- [5] M. Debost, P.B. Klar, N. Barrier, E.B. Clatworthy, J. Grand, F. Laine, P. Brázda, L. Palatinus, N. Nesterenko, P. Boullay, S. Mintova, Synthesis of discrete CHA zeolite nanocrystals without organic templates for selective CO₂ capture, *Angew. Chem. Int. Ed.* 59 (2020) 23491–23495, <https://doi.org/10.1002/anie.202009397>.
- [6] Y. Ji, M. Zhang, K. Guan, J. Zhao, G. Liu, W. Jin, High-performance CO₂ capture through polymer-based ultrathin membranes, *Adv. Funct. Mater.* 29 (2019) 1900735, <https://doi.org/10.1002/adfm.201900735>.
- [7] A.E. Creamer, B. Gao, Carbon-based adsorbents for postcombustion CO₂ capture: a critical review, *Environ. Sci. Technol.* 50 (2016) 7276–7289, <https://doi.org/10.1021/acs.est.6b00627>.
- [8] H. Sun, J. Wang, J. Zhao, B. Shen, J. Shi, J. Huang, C. Wu, Dual functional catalytic materials of Ni over Ce-modified CaO sorbents for integrated CO₂ capture and conversion, *Appl. Catal. B* 244 (2019) 63–75, <https://doi.org/10.1016/j.apcatb.2018.11.040>.
- [9] G. Zhang, P. Zhao, Y. Xu, Z. Yang, H. Cheng, Y. Zhang, Structure property - CO₂ capture performance relations of amine-functionalized porous silica composite adsorbents, *ACS Appl. Mater. Interfaces* 10 (2018) 34340–34354, <https://doi.org/10.1021/acsami.8b13069>.
- [10] J. Yoon, H.-S. Yang, B.-S. Lee, W.-R. Yu, Recent progress in coaxial electrospinning: new parameters, various structures, and wide applications, *Adv. Mater.* 30 (2018) 1704765, <https://doi.org/10.1002/adma.201704765>.
- [11] H.-Y. Mi, X. Jing, Q. Zheng, L. Fang, H.-X. Huang, L.-S. Turng, S. Gong, High-performance flexible triboelectric nanogenerator based on porous aerogels and electrospun nanofibers for energy harvesting and sensitive self-powered sensing, *Nano Energy* 48 (2018) 327–336, <https://doi.org/10.1016/j.nanoen.2018.03.050>.
- [12] Y. Zhang, B.-T. Zhang, Y. Teng, J. Zhao, X. Sun, Heterogeneous activation of persulfate by carbon nanofiber supported Fe₃O₄@carbon composites for efficient ibuprofen degradation, *J. Hazard. Mater.* 401 (2021), 123428, <https://doi.org/10.1016/j.jhazmat.2020.123428>.
- [13] S. Kang, D.H. Park, J. Hwang, Hierarchical ZnO nano-spines grown on a carbon fiber seed layer for efficient VOC removal and airborne virus and bacteria inactivation, *J. Hazard. Mater.* 424 (2022), 127262, <https://doi.org/10.1016/j.jhazmat.2021.127262>.
- [14] L. Zhang, T. Wei, Z. Jiang, C. Liu, H. Jiang, J. Chang, L. Sheng, Q. Zhou, L. Yuan, Z. Fan, Electrostatic interaction in electrospun nanofibers: Double-layer carbon protection of CoFe₂O₄ nanosheets enabling ultralong-life and ultrahigh-rate lithium ion storage, *Nano Energy* 48 (2018) 238–247, <https://doi.org/10.1016/j.nanoen.2018.03.053>.
- [15] X. Li, W. Chen, Q. Qian, H. Huang, Y. Chen, Z. Wang, Q. Chen, J. Yang, J. Li, Y. W. Mai, Electrospinning-based strategies for battery materials, *Adv. Energy Mater.* 11 (2021) 2000845, <https://doi.org/10.1002/aenm.202000845>.
- [16] S. Kang, J. Choi, G.Y. Park, H.R. Kim, J. Hwang, A novel and facile synthesis of Ag-doped TiO₂ nanofiber for airborne virus/bacteria inactivation and VOC elimination under visible light, *Appl. Surf. Sci.* 599 (2022), 153930, <https://doi.org/10.1016/j.apsusc.2022.153930>.
- [17] C. Yang, B. Wang, Y. Zhang, H. Wang, Preparation and properties of polyacrylonitrile fibers with guanidine groups, *Fibers Polym.* 16 (2015) 1611–1617, <https://doi.org/10.1007/s12221-015-4480-1>.
- [18] Z. Liu, Q. Wang, J. Wu, H. Zhang, Y. Liu, T. Zhang, H. Tian, S. Zeng, Active sites and interfacial reducibility of Cu₂O/CeO₂ catalysts induced by reducing media and O₂/H₂ activation, *ACS Appl. Mater. Interfaces* 13 (2021) 35804–35817, <https://doi.org/10.1021/acsami.1c09332>.
- [19] W. Li, L. Jin, F. Gao, H. Wan, Y. Pu, X. Wei, C. Chen, W. Zou, C. Zhu, L. Dong, Advantageous roles of phosphate decorated octahedral CeO₂ {1 1 1}-g-C₃N₄ in boosting photocatalytic CO₂ reduction: charge transfer bridge and Lewis basic site, *Appl. Catal. B* 294 (2021), 120257, <https://doi.org/10.1016/j.apcatb.2021.120257>.
- [20] M.S.A. Rahaman, A.F. Ismail, A. Mustafa, A review of heat treatment on polyacrylonitrile fiber, *Polym. Degrad. Stab.* 92 (2007) 1421–1432, <https://doi.org/10.1016/j.polymdegradstab.2007.03.023>.
- [21] S. Kang, J. Hwang, Fabrication of hollow activated carbon nanofibers (HACNFs) containing manganese oxide catalyst for toluene removal via two-step process of electrospinning and thermal treatment, *Chem. Eng. J.* 379 (2020), 122315, <https://doi.org/10.1016/j.cej.2019.122315>.

- [22] D. Ye, R. Wang, X. Wang, X. Liu, H. Liu, H. Wang, Effects of synthesis methods on the physicochemical properties and Hg^0 capture capability of $\text{MnO}_2\text{-CeO}_2$ mixed oxides, *Appl. Surf. Sci.* 578 (2022), 151998, <https://doi.org/10.1016/j.apsusc.2021.151998>.
- [23] A.C. Dassanayake, M. Jaroniec, Dual optimization of microporosity in carbon spheres for CO_2 adsorption by using pyrrole as the carbon precursor and potassium salt as the activator, *J. Mater. Chem. A* 5 (2017) 19456–19466, <https://doi.org/10.1039/C7TA05523D>.
- [24] X. Zhao, X. Zeng, Y. Qin, X. Li, T. Zhu, X. Tang, An experimental and theoretical study of the adsorption removal of toluene and chlorobenzene on coconut shell derived carbon, *Chemosphere* 206 (2018) 285–292, <https://doi.org/10.1016/j.chemosphere.2018.04.126>.
- [25] X. Yao, R. Zhao, L. Chen, J. Du, C. Tao, F. Yang, L. Dong, Selective catalytic reduction of NO_x by NH_3 over CeO_2 supported on TiO_2 : Comparison of anatase, brookite, and rutile, *Appl. Catal. B* 208 (2017) 82–93, <https://doi.org/10.1016/j.apcatb.2017.02.060>.
- [26] J. Kong, S. Yu, Fourier transform infrared spectroscopic analysis of protein secondary structures, *Acta Biochim. Biophys. Sinica* 39 (2007) 549–559, <https://doi.org/10.1111/j.1745-7270.2007.00320.x>.
- [27] W. Xu, B. Xin, X. Yang, Carbonization of electrospun polyacrylonitrile (PAN)/cellulose nanofibril (CNF) hybrid membranes and its mechanism, *Cellulose* 27 (2020) 3789–3804, <https://doi.org/10.1007/s10570-020-03006-y>.
- [28] X. Zheng, Y. Li, L. Zhang, L. Shen, Y. Xiao, Y. Zhang, C. Au, L. Jiang, Insight into the effect of morphology on catalytic performance of porous CeO_2 nanocrystals for H_2S selective oxidation, *Appl. Catal. B* 252 (2019) 98–110, <https://doi.org/10.1016/j.apcatb.2019.04.014>.
- [29] L. Lin, S. Yao, Z. Liu, F. Zhang, N. Li, D. Vovchok, A. Martínez-Arias, R. Catedana, J. Lin, S.D. Senanayake, D. Su, D. Ma, J.A. Rodriguez, In situ characterization of Cu/CeO_2 nanocatalysts for CO_2 hydrogenation: Morphological effects of nanostructured ceria on the catalytic activity, *J. Phys. Chem. C* 122 (2018) 12934–12943, <https://doi.org/10.1021/acs.jpcc.8b03596>.
- [30] W.-F. Kuan, W.-Y. Yu, F.-Y. Tu, C.-H. Chung, Y.-C. Chang, M.M. Lin, T.-H. Yu, L.-J. Chen, Facile reflux preparation of defective mesoporous ceria nanorod with superior catalytic activity for direct carbon dioxide conversion into dimethyl carbonate, *Chem. Eng. J.* 430 (2022), 132941, <https://doi.org/10.1016/j.cej.2021.132941>.
- [31] Y. Liu, J. Wilcox, Molecular simulation studies of CO_2 adsorption by carbon model compounds for carbon capture and sequestration applications, *Environ. Sci. Technol.* 47 (2013) 95–101, <https://doi.org/10.1021/es3012029>.
- [32] F.E.C. Othman, N. Yusof, M. Petri, N.A.H.M. Nordin, M.F. Hamid, A.F. Ismail, A. I. Rushdan, S.A. Hassan, Polyethyleneimine-impregnated activated carbon nanofiber composited graphene-derived rice husk char for efficient post-combustion CO_2 capture, *Nanotechnol. Rev.* 11 (2022) 926–944, <https://doi.org/10.1515/ntrev-2022-0055>.
- [33] X. Yan, L. Zhang, Y. Zhang, K. Qiao, Z. Yan, S. Komarneni, Amine-modified mesocellular silica foams for CO_2 capture, *Chem. Eng. J.* 168 (2011) 918–924, <https://doi.org/10.1016/j.cej.2011.01.066>.
- [34] P. Hu, J. An, M.M. Faulkner, H. Wu, Z. Li, X. Tian, J.P. Giraldo, Nanoparticle charge and size control foliar delivery efficiency to plant cells and organelles, *ACS Nano* 14 (2020) 7970–7986, <https://doi.org/10.1021/acsnano.9b09178>.
- [35] J. Li, Z. Xia, Q. Xue, M. Zhang, S. Zhang, H. Xiao, Y. Ma, Y. Qu, Insights into the interfacial Lewis acid-base pairs in CeO_2 -loaded CoS_2 electrocatalysts for alkaline hydrogen evolution, *Small* 17 (2021) 2103018, <https://doi.org/10.1002/sml.202103018>.
- [36] F. Gu, K. Chen, Y. Du, Y. Song, L. Wang, $\text{CeO}_2\text{-NiO/N}$, O-rich porous carbon derived from covalent-organic framework for enhanced Li-storage, *Chem. Eng. J.* 442 (2022), 136298, <https://doi.org/10.1016/j.cej.2022.136298>.
- [37] R. Sanz, G. Calleja, A. Arencibia, E.S. Sanz-Pérez, CO_2 adsorption on branched polyethyleneimine-impregnated mesoporous silica SBA-15, *Appl. Surf. Sci.* 256 (2010) 5323–5328, <https://doi.org/10.1016/j.apsusc.2009.12.070>.
- [38] R. Kishor, A.K. Ghoshal, High molecular weight polyethyleneimine functionalized three dimensional mesoporous silica for regenerable CO_2 separation, *Chem. Eng. J.* 300 (2016) 236–244, <https://doi.org/10.1016/j.cej.2016.04.055>.
- [39] F. Liu, S. Chen, Y. Gao, Synthesis of porous polymer based solid amine adsorbent: effect of pore size and amine loading on CO_2 adsorption, *J. Colloid Interface Sci.* 506 (2017) 236–244, <https://doi.org/10.1016/j.jcis.2017.07.049>.
- [40] V.K. Singh, E.A. Kumar, Comparative studies on CO_2 adsorption isotherms by solid adsorbents, *Mater. Today Proc.* 5 (2018) 23033–23042, <https://doi.org/10.1016/j.matpr.2018.11.032>.
- [41] A. Sarwar, M. Ali, A.H. Khoja, A. Nawar, A. Waqas, R. Liaquat, S.R. Naqvi, M. Asjid, Synthesis and characterization of biomass-derived surface-modified activated carbon for enhanced CO_2 adsorption, *J. CO₂ Util.* 46 (2021) 101476, <https://doi.org/10.1016/j.jcou.2021.101476>.
- [42] C. Słostowski, S. Marre, P. Dagault, O. Babet, T. Toupance, C. Aymonier, CeO_2 nanopowders as solid sorbents for efficient CO_2 capture/release processes, *J. CO₂ Util.* 20 (2017) 52–58, <https://doi.org/10.1016/j.jcou.2017.03.023>.
- [43] Q. Li, J. Guo, D. Xu, J. Guo, X. Ou, Y. Hu, H. Qi, F. Yan, Electrospun N-doped porous carbon nanofibers incorporated with NiO nanoparticles as free-standing film electrodes for high-performance supercapacitors and CO_2 capture, *Small* 14 (2018) 1704203, <https://doi.org/10.1002/sml.201704203>.
- [44] F.E.C. Othman, N. Yusof, S. Samitsu, N. Abdullah, M.F. Hamid, K. Nagai, M.N.Z. Abidin, M.A. Azali, A.F. Ismail, J. Jaafar, F. Aziz, W.N.W. Salleh, Activated carbon nanofibers incorporated metal oxides for CO_2 adsorption: effects of different type of metal oxides, *J. CO₂ Util.* 45 (2021) 101434, <https://doi.org/10.1016/j.jcou.2021.101434>.
- [45] M. Niu, H. Yang, X. Zhang, Y. Wang, A. Tang, Amine-impregnated mesoporous silica nanotube as an emerging nanocomposite for CO_2 capture, *ACS Appl. Mater. Interfaces* 8 (2016) 17312–17320, <https://doi.org/10.1021/acsami.6b05044>.
- [46] V. Irani, A.G. Khosh, A. Tavasoli, Polyethyleneimine (PEI) functionalized metal oxide nanoparticles recovered from the catalytic converters of spent automotive exhaust systems and application for CO_2 adsorption, *Front. Energy Res.* 8 (2020) 196, <https://doi.org/10.3389/fenrg.2020.00196>.
- [47] B. Wu, F.Q. Liu, S.W. Luo, L.Q. Zhang, F. Zou, Carbonaceous materials-supported polyethyleneimine with high thermal conductivity: a promising adsorbent for CO_2 capture, *Compos. Sci. Technol.* 208 (2021), 108781, <https://doi.org/10.1016/j.compscitech.2021.108781>.
- [48] K. Li, J. Jiang, F. Yan, S. Tian, X. Chen, The influence of polyethyleneimine type and molecular weight on the CO_2 capture performance of PEI-nano silica adsorbents, *Appl. Energy* 136 (2014) 750–755, <https://doi.org/10.1016/j.apenergy.2014.09.057>.
- [49] B. Stieberova, M. Zilka, M. Ticha, F. Freiberg, P. Caramazana-González, J. McKechnie, E. Lester, Sustainability assessment of continuous-flow hydrothermal synthesis of nanomaterials in the context of other production technologies, *J. Clean. Prod.* 241 (2019), 118325, <https://doi.org/10.1016/j.jclepro.2019.118325>.
- [50] Z.C. Sims, M.S. Kesler, H.B. Henderson, E. Castillo, T. Fishman, D. Weiss, P. Singleton, R. Eggert, S.K. McCall, O. Rios, How cerium and lanthanum as coproducts promote stable rare earth production and new alloys, *J. Sustain. Metall.* 8 (2022) 1225–1234, <https://doi.org/10.1007/s40831-022-00562-4>.